ABSTRACT

THOMPSON, KYLE B. Aerothermodynamic Design Sensitivities for a Reacting Gas Flow Solver on an Unstructured Mesh Using a Discrete Adjoint Formulation. (Under the direction of Hassan Hassan and Peter Gnoffo.)

Approach is described to efficiently compute aerothermodynamic design sensitivities using a decoupled approach. In this approach, the species continuity equations are decoupled from the mixture continuity, momentum, and total energy equations for the Roe flux difference splitting scheme in both the flow and adjoint solvers. This decoupling simplifies the implicit system, so that the flow solver can be made significantly more efficient, with very little penalty on overall scheme robustness. Most importantly, the computational cost of the point implicit relaxation is shown to scale linearly with the number of species for the decoupled system, whereas the fully coupled approach scales quadratically. Also, the decoupled method significantly reduces the cost in wall time and memory in comparison to the fully coupled approach.

A design optimization of a re-entry vehicle with a annular nozzle on the forebody is completed based on this approach. The sensitivities of the drag coefficient and surface temperature with respect to a plenum inboard the vehicle were computed and verified against complex-variable finite-difference.

Aerothermodynamic Design Sensitivities for a Reacting Gas Flow Solver
on an Unstructured Mesh Using a Discrete Adjoint Formulation

by
Kyle B. Thompson

A dissertation submitted to the Graduate Faculty of
North Carolina State University
in partial fulfillment of the
requirements for the Degree of
Doctor of Philosophy

Aerospace Engineering

Raleigh, North Carolina

2016

APPROVED BY:

_____
Hassan Hassan
Co-chair of Advisory Committee

_____
Peter Gnoffo
Co-chair of Advisory Committee

_____
Jack Edwards

_____
Hong Luo

_____
John Griggs

DEDICATION

To my parents and friends.

BIOGRAPHY

The author was born on December 11th, 1990, in Willow Springs, North Carolina. He recieved a BS in Aerospace Engineering from North Carolina State University in 2012, and subsequently recieved his MS in Aerospace Engineering from North Carolina State University in 2014. After recieving he MS, he began work in the Aerothermodynamics branch of NASA Langley Research Center, via the Pathways program. He completed this disseration on adjoint-based optimization while working at NASA Langley Research Center.

ACKNOWLEDGEMENTS

TABLE OF CONTENTS

LIST OF TABLES

LIST OF FIGURES

Chapter 1

Introduction

In the last decades computational fluid dynamics (CFD) codes have matured to the point that it is possible to obtain high-fidelity design sensitivities that can be coupled with optimization packages to enable design optimization for a variety of design inputs[5, 3]. In recent years, the benefits of using an adjoint-based formulation to compute sensitivities have been realized and implemented in many compressible CFD codes[24, 25, 27], because of the ability compute all sensitivities at the cost of a single extra adjoint solution, instead of an additional flow solution for each design variable. Reacting gas CFD codes have lagged significantly in adopting this adjoint-based approach, with only a small number of codes having published results[10, 11]. This is likely due to the significant jump in complexity of the linearizations required, especially in regard to the chemical source term and the dissipation term in the Roe flux difference splitting (FDS) scheme[30].

An additional obstacle that may prevent adjoint-based sensitivity analysis in reacting gas solvers is the extreme problem size associated with high energy physics. The additional equations required in reacting gas simulations lead to large Jacobians that scale quadratically in size to the number of governing equations. This leads to a significant increase in the memory required to store the flux linearizations and the computational cost of the point solver. As reacting gas CFD solvers are used to solve increasingly more complex problems, this onerous quadratic scaling of computational cost and Jacobian size will ultimately surpass the current limits of hardware and time constraints on achieving a flow solution[12].

To mitigate this scaling issue, Candler et al.[9] proposed a scheme to for a modified form of the Steger-Warming flux vector splitting scheme[23, 33]. In that work, it was shown that quadratic scaling between the cost of solving the implicit system and adding species mass equations can be reduced from quadratic to linear scaling by decoupling the species mass equations from the mixture mass, momentum, and energy equations and solving the two systems sequentially. This work extends the aforementioned work from the modified form of the Steger-

Warming flux vector splitting method to the Roe flux difference splitting (FDS) scheme.

The work presented demonstrates that this decoupling can be applied to both the flow solver and adjoint solver in a reacting gas CFD code, and significantly improve the efficiency in both computational cost and memory required. Additionally the implementation of exact linearizations is shown to significantly improve performance and robustness in the flow solver over common approximations used when linearizing the Roe FDS scheme. The formulation and linearization of the fluxes for the Roe FDS scheme are presented here, and design optimization for an inviscid reacting flow is conducted for inviscid, reacting flow around an axi-symmetric hypersonic re-entry vehicle with an annular jet.

Chapter 2

Governing Equations

In this section, the conservative equations governing fluid flow for inviscid, chemically reacting flow are presented. This research is extendable to multi-temperature models to account for higher excitation modes than the translational mode; however, the focus of this research uses a 1-temperature model, so only a single, total energy equation is used. The thermodynamic relations and chemical kinetics models used are also presented in detail here.

2.1 Reacting Flow Conservation Equations

Conservation equations for a fluid mixture that is chemical non-equilibrium and thermal equilibrium can be written as

Species Conservation :

$$\frac{\partial \rho_s}{\partial t} + \frac{\partial \rho_s u}{\partial x} + \frac{\partial \rho_s v}{\partial y} + \frac{\partial \rho_s w}{\partial z} = w_s$$

(2.1)

Mixture Momentum Conservation :

$$\frac{\partial \rho u}{\partial t} + \frac{\partial \rho u^2}{\partial x} + \frac{\partial \rho uv}{\partial y} + \frac{\partial \rho uw}{\partial z} = -\frac{\partial p}{\partial x}$$

$$\frac{\partial \rho v}{\partial t} + \frac{\partial \rho vu}{\partial x} + \frac{\partial \rho v^2}{\partial y} + \frac{\partial \rho vw}{\partial z} = -\frac{\partial p}{\partial y}$$

$$\frac{\partial \rho w}{\partial t} + \frac{\partial \rho wu}{\partial x} + \frac{\partial \rho wv}{\partial y} + \frac{\partial \rho w^2}{\partial z} = -\frac{\partial p}{\partial z}$$

(2.2)

Total Energy Conservation :

$$\frac{\partial \rho E}{\partial t} + \frac{\partial \rho \left(E + p\right) u}{\partial x} + \frac{\partial \rho \left(E + p\right) v}{\partial y} + \frac{\partial \rho \left(E + p\right) w}{\partial z} = 0$$

(2.3)

2.2 Thermodynamic Relationships

The pressure, p, is defined as the sum of the partial pressures of the species

$$p = \sum_{s=1}^{N_s} p_s \tag{2.4}$$

and the partial pressure of species s, p_s, is defined as

$$p_s = \frac{\rho_s R_u T}{M_s} \tag{2.5}$$

where R_u is the universal gas constant and M_s is the molecular weight of species s. The total energy per unit mass E, is defined as

$$E = \sum c_s e_s + \frac{u^2 + v^2 + w^2}{2} \tag{2.6}$$

where c_s is the mass fraction of species s, defined as

$$c_s = \frac{\rho_s}{\rho} \tag{2.7}$$

and e_s is the specific internal energy of species s, defined as

$$e_s = \int_{T_{ref}}^{T} C_{v,s} \, dT + e_{s,o} \tag{2.8}$$

where T_ref is a reference temperature, with $e_{s,o}$ being the specific internal energy. In practice, the specific heat at constant volume for species s, $C_{v,s}$, is not used directly. Instead, the specific heat at constant pressure for species s, $C_{p,s}$, is determined via thermodynamic curve fits and related to $C_{v,s}$ via

$$C_{v,s} = C_{p,s} - \frac{R_u}{M_s} \tag{2.9}$$

The thermodynamic properties curve fit tables developed by McBride, Gordon, and Reno[6] were used to compute $C_{p,s}$, and quadratic blending function was used to ensure that $C_{p,s}$ and enthalpy were continuous across temperature ranges. The details of this blending are given in Appendix A.

2.3 Chemical Kinetics Model

The production and destruction of species is governed by the source terms, w_s, defined as

$$w_s = M_s \sum_{r=1}^{N_r} \left(\nu''_{s,r} - \nu'_{s,r} \right) \left(R_{f,r} - R_{b,r} \right) \tag{2.10}$$

where N_r is the number of reactions, $\nu'_{s,r}$ and $\nu''_{s,r}$ are the stoichiometric coefficients for the reactants and products, respectively, and $R_{f,r}$ and $R_{b,r}$ are the forward and backward rates for reaction r, respectively. The forward and backward reaction rates are defined as

$$R_{f,r} = 1000 \left[k_{f,r} \prod_{s=1}^{N_s} \left(0.001 \rho_s / M_s \right) \nu'_{s,r} \right] \tag{2.11}$$

$$R_{b,r} = 1000 \left[k_{b,r} \prod_{s=1}^{N_s} \left(0.001 \rho_s / M_s \right) \nu''_{s,r} \right] \tag{2.12}$$

where $k_{f,r}$ and $k_{b,r}$ are the forward and backward rate coefficients, respectively. It should be noted that all terms on the RHS for Eq.s (2.11-2.12) are in cgs units. The factors 1000 and 0.001 are required to convert from cgs to mks, so that $R_{f,r}$ and $R_{b,r}$ are in mks units. The rate coefficients are expressed in the manner defined by Park[29], but for a one-temperature model; thus, the forward and back rate coefficients are defined as

$$k_{f,r} = C_{f,r} T^{n_{f,r}} exp \left(-E_{f,r} / kT \right) \tag{2.13}$$

$$k_{b,r} = \frac{k_{f,r}}{K_{c,r}} \tag{2.14}$$

where $K_{c,r}$ is the equilibrium constant for reaction r, and k is the Boltzmann constant. The preexponential factors $C_{f,r}$ and $n_{f,r}$, as well as the activation energy, E_f, are documented by Gnoffo[20]. The equilibrium coefficient is computed according to the curve fit defined by Park[28]

$$K_{c,r} = exp(B_1^r + B_2^r \ln Z + B_3^r Z + B_4^r Z^2 + B_5^r Z^3) \tag{2.15}$$

$$Z = 10000/T \tag{2.16}$$

where the curve fit constants, B_i^r, are also documented by Gnoffo[20]

Chapter 3

Numerical Solution of Flow Equations

3.1 Fully-Coupled Point Implicit Method

The governing equations presented in Eq.s (2.1-2.3) can be recast in vector form as

$$\frac{\partial \mathbf{U}}{\partial t} + \nabla \cdot \mathbf{F} = \mathbf{W} \tag{3.1}$$

or, in semi-discrete form,

$$\frac{\partial \mathbf{U}}{\partial t} + \frac{1}{V} \sum_f (\mathbf{F} \cdot \mathbf{S})^f = \mathbf{W} \tag{3.2}$$

summing over all faces, f, in the domain, where V is the cell volume, $\mathbf{W}$ is the chemical source term vector, and $\mathbf{S}$ is the face outward normal vector. The vectors of conserved variables and fluxes are:

$$\mathbf{U} = \begin{pmatrix} \rho_1 \\ \vdots \\ \rho_{ns} \\ \rho u \\ \rho v \\ \rho w \\ \rho E \end{pmatrix}, \quad \mathbf{F} = \begin{pmatrix} \rho_1 \overline{U} \\ \vdots \\ \rho_{ns} \overline{U} \\ \rho u \overline{U} + p s_x \\ \rho u \overline{U} + p s_y \\ \rho u \overline{U} + p s_z \\ (\rho E + p) \overline{U} \end{pmatrix} \tag{3.3}$$

where $\overline{U}$ is the outward pointing normal velocity, E is the total energy of the mixture per unit mass as defined in Eq. 2.6, and e_s is the internal energy of species s as defined in Eq. 2.8. By

using the Roe FDS scheme,

$$\mathbf{F}^{n+1} \approx \mathbf{F}^n + \frac{\partial \mathbf{F}}{\partial \mathbf{U}} \delta \mathbf{U}^n$$

$$\mathbf{W}^{n+1} \approx \mathbf{W}^n + \frac{\partial \mathbf{W}}{\partial \mathbf{U}} \delta \mathbf{U}^n$$

(3.4)

where $\delta \mathbf{U}^n = \mathbf{U}^{n+1} - \mathbf{U}^n$. By using an implicit time integration, the implicit scheme becomes:

$$\frac{\delta \mathbf{U}^n}{\Delta t} + \frac{1}{V} \sum_f \left(\frac{\partial \mathbf{F}^f}{\partial \mathbf{U^L}} \delta \mathbf{U}^L + \frac{\partial \mathbf{F}^f}{\partial \mathbf{U^R}} \delta \mathbf{U}^R \right)^n \mathbf{S}^f - \frac{\partial \mathbf{W}}{\partial \mathbf{U}} \delta \mathbf{U}^n = -\frac{1}{V} \sum_f (\mathbf{F}^f \cdot \mathbf{S}^f)^n + \mathbf{W}^n \qquad (3.5)$$

or, put more simply:

$$A \delta \mathbf{U}^n = \mathbf{b} \qquad (3.6)$$

where A is the Jacobian matrix of the fully coupled system, and $\mathbf{b}$ is the residual vector. For a point implicit relaxation scheme, the Jacobian matrix can be split into its diagonal and off-diagonal elements, with the latter moved to the RHS:

$$A = O + D \qquad (3.7)$$

Each matrix element is a square $(ns+4) \times (ns+4)$ matrix. One method of solving this system is a Red-Black Gauss-Seidel scheme[31], where matrix coefficients with even indices are updated first and, subsequently, the coefficients with odd indices are updated. This red-black ordering enables better vectorization in solving the linear system. The computational work for the Gauss-Seidel scheme is dominated by matrix-vector multiplications of elements of O with $\delta \mathbf{U}$, which are $O(N^2)$ operations, where $N = ns + 4$. In the next section, it is shown that decoupling the system reduces these matrix-vector multiplications to $O(N^2 + M)$ operations, where $N = ns$ and $M = ns$.

3.2 Decoupled Point Implicit Method

If the species mass equations are replaced by a single mixture mass equation, the mixture equations can be separated from the species mass equations and the conserved variables become

$$\mathbf{U}' = \begin{pmatrix} \rho \\ \rho u \\ \rho v \\ \rho w \\ \rho E \end{pmatrix} \qquad \hat{\mathbf{U}} = \begin{pmatrix} \rho_1 \\ \vdots \\ \rho_{ns} \end{pmatrix} \qquad (3.8)$$

Solving the flux vector is performed in two sequential steps. The mixture fluxes are first solved as

$$\frac{\partial \mathbf{U}'}{\partial t} + \frac{1}{V} \sum_f (\mathbf{F}' \cdot \mathbf{S})^f = 0 \tag{3.9}$$

followed by the species fluxes as

$$\frac{\partial \hat{\mathbf{U}}}{\partial t} + \frac{1}{V} \sum_f (\hat{\mathbf{F}} \cdot \mathbf{S})^f = \hat{\mathbf{W}} \tag{3.10}$$

Point relaxation uses Red-Black Gauss-Seidel to update the conserved variables in $\mathbf{U}'$ and all associated auxiliary variables, such as temperature, pressure, speed of sound, etc. This is done by holding the thermo-chemical state constant, and will always result in the relaxation of a five-equation system. This does trade an implicit relationship between the mixture and species equations for an explicit one; thus, this decoupling can have an impact on the stability of the scheme, especially due to the non-linearity of the chemical source term[29].

The solution of the species mass equations takes a different form. Based on the work of Candler et al.[9], the decoupled variables can be rewritten in terms of mass fraction, as follows:

$$\delta \hat{\mathbf{U}}^n = \rho^{n+1} \hat{\mathbf{V}}^{n+1} - \rho^n \hat{\mathbf{V}}^n = \rho^{n+1} \delta \hat{\mathbf{V}}^n + \hat{\mathbf{V}}^n \delta \rho^n \tag{3.11}$$

where $\hat{\mathbf{V}} = (c_1, \ldots, c_{ns})^T$, and $c_s = \rho_s/\rho$ the mass fraction of species s. While the derivation of the species mass equations is different for the Roe FDS scheme from that of Steger-Warming proposed by Candler et al.[9], the final result takes a similar form:

$$\hat{F}_{\rho_s} = c_s F'_\rho + (c_s^L - \tilde{c}_s) \rho^L \lambda^+ + (c_s^R - \tilde{c}_s) \rho^R \lambda^- \tag{3.12}$$

where F'_ρ is the total mass flux computed previously using all $\mathbf{U}'$ variables, and ˜denotes a Roe-averaged quantity. Likewise, linearizing the species mass fluxes with respect to the $\hat{\mathbf{V}}$ variables yields

$$\hat{\mathbf{F}}^{n+1} = \hat{\mathbf{F}}^n + \frac{\partial \hat{\mathbf{F}}}{\partial \hat{\mathbf{V}}^L} \delta \hat{\mathbf{V}}^L + \frac{\partial \hat{\mathbf{F}}}{\partial \hat{\mathbf{V}}^R} \delta \hat{\mathbf{V}}^R \tag{3.13}$$

$$\frac{\partial \hat{\mathbf{F}}}{\partial \hat{\mathbf{V}}^L} = w F_\rho + (1-w)\rho^L \lambda^+ - w\rho^R \lambda^- \tag{3.14}$$

$$\frac{\partial \hat{\mathbf{F}}}{\partial \hat{\mathbf{V}}^R} = (1-w) F_\rho + (w-1)\rho^L \lambda^+ + w\rho^R \lambda^- \tag{3.15}$$

A full derivation of Eq.s (3.12-3.15), along with the definition of w, is included in Appendix A. The chemical source term is linearized in the same manner as the fully coupled scheme;

however, the updated $\mathbf{U}'$ variables are used to evaluate the Jacobian, and the chain rule is applied to linearize $\hat{\mathbf{W}}$ with respect to the species mass fractions:

$$\hat{\mathbf{W}}^{n+1} = \hat{\mathbf{W}}^n + \frac{\partial \hat{\mathbf{W}}}{\partial \mathbf{U}}\bigg|_{\mathbf{U}'} \frac{\partial \mathbf{U}}{\partial \hat{\mathbf{V}}} \tag{3.16}$$

For simplicity of notation, we define

$$C = \frac{\partial \hat{\mathbf{W}}}{\partial \mathbf{U}}\bigg|_{\mathbf{U}'} \frac{\partial \mathbf{U}}{\partial \hat{\mathbf{V}}} \tag{3.17}$$

The decoupled system to be solved becomes:

$$\rho^{n+1} \frac{\delta \hat{\mathbf{V}}^n}{\Delta t} + \frac{1}{V} \sum_f \left(\frac{\partial \hat{\mathbf{F}}^f}{\partial \hat{\mathbf{V}}^L} \delta \hat{\mathbf{V}}^L + \frac{\partial \hat{\mathbf{F}}^f}{\partial \hat{\mathbf{V}}^R} \delta \hat{\mathbf{V}}^R \right)^{n,n+1} \mathbf{S}^f - C^{n,n+1} \delta \mathbf{V}^n$$

$$= -\frac{1}{V} \sum_f (\hat{\mathbf{F}}^{n,n+1} \cdot \mathbf{S})^f + \mathbf{W}^{n,n+1} - \hat{\mathbf{V}}^n \frac{\delta \rho^n}{\Delta t} - R_\rho \tag{3.18}$$

$$R_\rho = -\frac{1}{V} \sum_f \sum_s (\hat{F}_{\rho_s}^{n,n+1} \cdot \mathbf{S}) \tag{3.19}$$

where R_ρ is included to preserve the constraint that the mass fractions sum to unity, i.e., $\sum_s c_s = 1$, $\sum_s \delta c_s = 0$.

3.3 Predicted Cost and Memory Savings of the Decoupled Implicit Problem

In decoupling the species equations, the most significant savings comes from the source term linearization being purely node-based[20]. Solving the mean flow equations is conducted in the same manner as the fully coupled system. All entries in the Jacobian A_m are linearizations of the mixture equation fluxes, which results in 5×5 matrices. All entries in the Jacobian A_d are linearizations of the species mass fluxes, which results in $ns \times ns$ matrices. Because there is no interdependence of species, except through the chemical source term, all contributions due to linearizing the convective flux are purely diagonal $ns \times ns$ matrices. Via Eq. 3.7, we decompose

9

A_d into its diagonal and off-diagonal elements, resulting in the following linear system:

$$\begin{pmatrix} \square & & & & \\ & \ddots & & & \\ & & \square & & \\ & & & \ddots & \\ & & & & \square \end{pmatrix} \begin{pmatrix} \delta\hat{\mathbf{V}}_1 \\ \vdots \\ \delta\hat{\mathbf{V}}_i \\ \vdots \\ \delta\hat{\mathbf{V}}_{nodes} \end{pmatrix} = \begin{pmatrix} \hat{b}_1 \\ \vdots \\ \hat{b}_i \\ \vdots \\ \hat{b}_{nodes} \end{pmatrix} - \begin{pmatrix} (\sum_{j=1}^{N_{nb}} \diagdown \delta\hat{\mathbf{V}}_j)_1 \\ \vdots \\ (\sum_{j=1}^{N_{nb}} \diagdown \delta\hat{\mathbf{V}}_j)_i \\ \vdots \\ (\sum_{j=1}^{N_{nb}} \diagdown \delta\hat{\mathbf{V}}_j)_{nodes} \end{pmatrix} \qquad (3.20)$$

where $\square$ represents a dense $ns \times ns$ matrix, $\diagdown$ represents a diagonal matrix, and $\delta\hat{\mathbf{V}}_j$ is the decoupled variable update on the node j that neighbors node i, where N_{nb} is the number of nodes neighboring node i. Thus, the non-zero entries in the off-diagonal matrix can be reduced from diagonal matrices to vectors. This results in significant savings in both computational cost and memory, as the only quadratic operation left in solving the implicit system is dealing with the diagonal entries in the Jacobian. Because the off-diagonal entries significantly outnumber the diagonal entries, we can expect nearly linear scaling in cost with the number of species. If compressed row storage[14] is used to only store non-zero off-diagonal entries, the relative memory savings in the limit of a large number of species for the Jacobian is given by

$$\begin{aligned} Relative\ Memory\ Cost &= \frac{size(A_d)}{size(A)} \\ &= \lim_{ns \to \infty} \frac{(ns^2 + 5^2)(N_{nodes}) + (ns + 5^2)(N_{nz})}{(ns + 4)^2(N_{nodes} + N_{nz})} \qquad (3.21) \\ &= \frac{N_{nodes}}{N_{nodes} + N_{nz}} \end{aligned}$$

where N_{nodes} is the number of nodes, and N_{nz} is the number of non-zero off-diagonal entries stored using compressed row storage. For a structured grid, each node has six neighbors in 3D, i.e., $N_{nz} = 6N_{nodes}$; therefore, we can expect the Jacobian memory required to decrease by a factor of seven using this decoupled scheme. Interestingly, for a grid that is not purely hexahedra, $N_{nz} > 6N_{nodes}$; thus, this decoupled scheme provides higher relative memory savings on unstructured grids than structured grids when using compressed row storage.

3.4   5 km/s Flow over Cylinder

Both the proposed decoupled scheme and the traditional, fully coupled approach have been implemented using FUN3D[2]. Demonstrating the improved efficiency in cost and memory required to utilize the decoupled scheme, and that both the fully coupled and decoupled approaches converge to the same result, a grid convergence study was conducted on a simple

cylinder geometry (radius 0.5 m). Due to the presence of strong shocks in blunt body flows, it was advantageous to generate structured-type grids to preserve grid alignment with the bow shock. A 50×50, 100×100, and 200×200 family of grids were adapted using the adaptation capability in FUN3D[4] to produce shock-aligned grids. These grids serve as a surrogate for conducting a grid convergence study, in that differences observed between the decoupled and fully coupled schemes decrease as the average mesh spacing decreases. These grids are unstructured, consisting totally of hexahedra elements with a single cell in the spanwise direction, and the 50×50 grid is shown in Figure 3.1. The cell elements of these grids were also subdivided into tetrahedral elements, and it was verified that there are no issues with a true unstructured grid topology. The free stream conditions used were $V_\infty = 5000 \ m/s$, $\rho_\infty = 0.001 \ kg/m^3$, and $T_\infty = 200 \ K$. Several chemical kinetics models were used, including a 5-species model with 5 reactions, an 11-species model with 22 reactions, and an 18-species model with 29 reactions. All cases were run in thermodynamic equilibrium, with a one-temperature model.
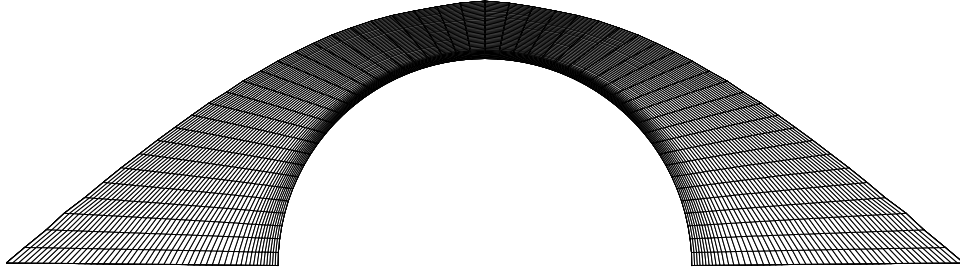
Figure 3.1: 50×50 cylinder grid.

3.4.1 Cylinder - Verification of Implementation

In order to be valid, the decoupled scheme must yield converged solutions that are nearly identical to those of the fully coupled system. To quantitatively assess this, we compare the predicted surface pressure, surface temperature, and the species composition on the stagnation line for both schemes. Figure 3.2 shows the predicted quantities on the 100×100 grid, for species mixture of N, N_2, O, O_2, and NO with five reactions. All results are indeed nearly identical,

with temperature and pressure matching discretely to eight digits and the species mass fractions on the stagnation line matching to four digits. This difference was further reduced on the finest grid level of 200×200, suggesting that both schemes converge to the same solution with grid refinement.

(a) Surface pressure   (b) Surface temperature   (c) Mass fractions on stagnation line
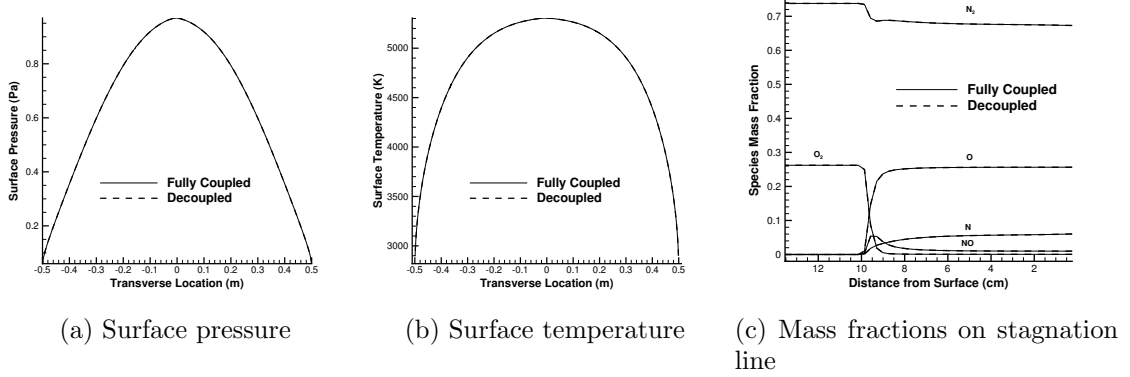
Figure 3.2: Cylinder predicted quantities.

3.4.2 Cylinder - Memory Cost

In order to determine the required memory of the decoupled scheme compared to the fully coupled scheme, a convergence study was conducted using Valgrind[1] to determine the memory actually allocated by FUN3D for an increasing number of species. Figure 3.3 shows that the relative memory cost converges asymptotically to $\sim 1/4$, which is nearly twice the predicted value of $1/7$. For the implementation of FUN3D, this is correct because the off-diagonal entries are reduced from double to single precision. Each structured grid node has six neighboring nodes, with the exception of those at the boundary. Because each of these six neighboring nodes yields single precision, off-diagonal Jacobian elements,

$$N_{nz} = \frac{6N_{nodes}}{2} = 3N_{nodes} \tag{3.22}$$

Substituting Eq. 3.22 into Eq. 3.21, the relative memory cost is:

$$Relative\ Memory\ Cost = \frac{N_{nodes}}{N_{nodes} + N_{nz}} = \frac{N_{nodes}}{N_{nodes} + (3N_{nodes})} = \frac{1}{4} \tag{3.23}$$

thus, the relative memory saved by using the decoupled scheme correctly approaches a factor

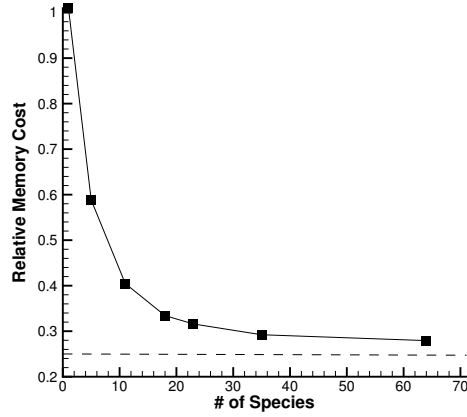Figure 3.3: Memory required convergence study

of 1/4.

3.4.3 Cylinder - Computational Cost

As stated before, the cost of solving the decoupled implicit system should scale approximately linearly with the number of species, whereas the fully coupled problem should scale quadratically; thus, the speedup of the implicit solve should be approximately linear when comparing the decoupled and fully coupled approaches. Figure 3.4 shows this to be true for the cylinder test case, and that the total speedup of the problem is less than that of just the linear solve. It is to be expected that the overall gains are not as large as those for the implicit solve, since there are many other factors that scale with the number of species, especially calculating the species source term and its linearization.

3.5   15 km/s Flow over Spherically-Capped Cone

To ensure that the decoupled scheme is robust and accurate at higher velocities, both the fully coupled and decoupled approaches were run on a sphere-cone geometry identical to that presented by Candler et. al. [9] (10 cm nose radius, 1.1 m length, 8° cone angle). For this case, a simple $64{\times}64$ hexahedra grid was constructed, and freestream conditions were set as $V_\infty = 15000\ m/s$, $\rho_\infty = 0.001\ kg/m^3$, $T_\infty = 200\ K$. It was discovered that CFL limitations for the decoupled scheme were prohibitive, because of the stiffness of the chemical source term. In order to converge the scheme in a manner competitive with the fully coupled approach, it was necessary to scale the magnitude of the source term contribution to the flux balance by a value ω, such that $0 \leq \omega \leq 1$. To ensure that the decoupled and fully coupled approaches yielded the
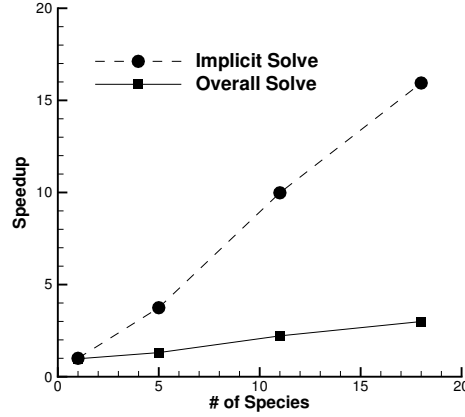
Figure 3.4: Relative speedup for the decoupled scheme vs. fully coupled scheme.

same result, a ramping scheme was implemented such that no scaling was performed on the source term when the solution was in a converged state.

3.5.1 Sphere-Cone - Verification of Implementation

As with the cylinder test case, the surface pressure and temperature were used as metrics to determine that both the decoupled and fully coupled approaches give the same answer when converged to steady-state. The species composition consisted of N, N_2, O, O_2, NO, N^+, N_2^+, O^+, O_2^+, NO^+, and electrons, with 22 possible reactions. Figure 3.5 shows that both methods again yield similar results, and the high stagnation temperature indicates that this is an inviscid, one-temperature simulation. This demonstrates that the decoupled approach is able to converge to the same solution as the fully coupled solution, in spite of the chemical reactions proceeding very rapidly due to a high stagnation temperature.

3.5.2 Sphere-Cone - Convergence Quality

The limits on the stability of the decoupled scheme derives from introducing explicitness in creating and destroying species. By scaling the magnitude of the chemical source term during the transient phase of the solve, this instability can be mitigated, and the convergence of decoupled scheme approaches that of the fully coupled scheme. Scaling of chemical source term was done identically between the decoupled and fully coupled scheme by ramping the factor ω from 0.001 to 1.0 over the first 500 timesteps. Figure 3.6 shows that the convergence of both schemes progresses nearly identically, with the decoupled scheme converging in significantly less computational time and, interestingly, fewer timesteps. This demonstrates that the decoupled

14
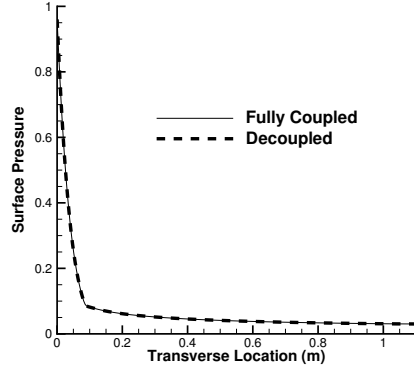
(a) Surface pressure
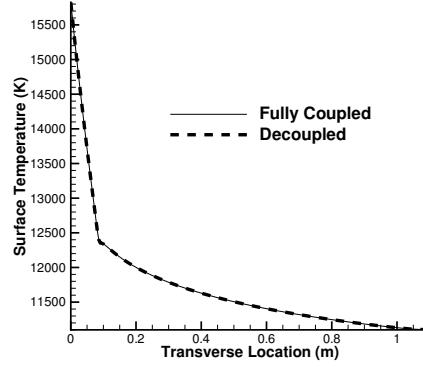
(b) Surface temperature

Figure 3.5: Sphere-cone predicted quantities.
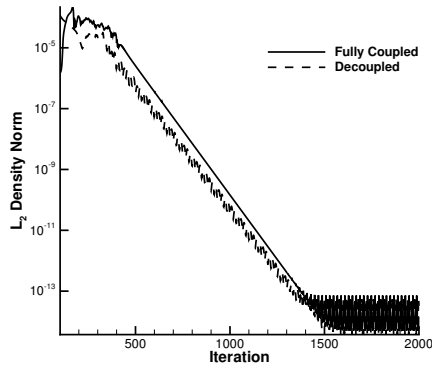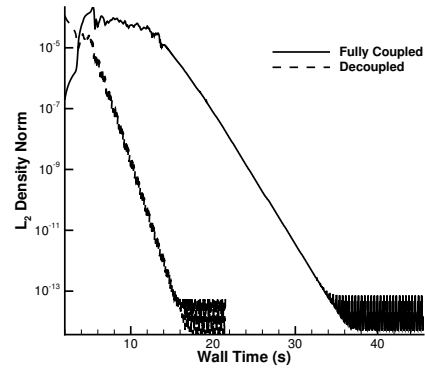

(a) Iterations to convergence

(b) Computational time to convergence

Figure 3.6: Sphere-cone convergence details.

15

scheme has significant potential to improve the efficiency of high-velocity simulations, and that the stiffness of the source term can be overcome in the presence of large chemical reaction rates.

Chapter 4

Numerical Solution of Adjoint Equations

This section details the derivation of the adjoint equations to be solved in conjunction with the primal flow equations. The primary goal of this research is to compute sensitivities of aerodynamic and aerothermodynamic quantities to design variables. To achieve this, the sensitivity to the primal flow equation formulation must first be solved. For a discrete adjoint formulation, this requires a solution of costate variables, relating a change in the flow equation residual to a change in the function of interest. Because of the large number of equations required in a reacting gas solver, the adjoint solver will suffer from the quadratic scaling in computational cost and memory required similarly to the primal flow solver. To mitigate this, a decoupled scheme is derived that is consistent with the decoupled flow solver.

4.1 Discrete Adjoint Derivation

The derivation for the discrete adjoint begins with forming the Lagrangian as

$$L(\mathbf{D}, \mathbf{Q}, \mathbf{X}, \boldsymbol{\Lambda}) = f(\mathbf{D}, \mathbf{Q}, \mathbf{X}) + \boldsymbol{\Lambda}^T \mathbf{R}(\mathbf{D}, \mathbf{Q}, \mathbf{X}) \tag{4.1}$$

Where $\mathbf{R}$ is the residual of the flow equations. Differentiating with respect to the design variables $\mathbf{D}$ yields

$$\frac{\partial L}{\partial \mathbf{D}} = \left\{ \frac{\partial f}{\partial \mathbf{D}} + \left[\frac{\partial \mathbf{X}}{\partial \mathbf{D}} \right]^T \frac{\partial f}{\partial \mathbf{X}} \right\} + \left[\frac{\partial \mathbf{Q}}{\partial \mathbf{D}} \right]^T \left\{ \frac{\partial f}{\partial \mathbf{Q}} + \left[\frac{\partial \mathbf{R}}{\partial \mathbf{Q}} \right]^T \boldsymbol{\Lambda} \right\} + \left\{ \left[\frac{\partial \mathbf{R}}{\partial \mathbf{D}} \right]^T + \left[\frac{\partial \mathbf{X}}{\partial \mathbf{D}} \right]^T \left[\frac{\partial \mathbf{R}}{\partial \mathbf{X}} \right]^T \right\} \boldsymbol{\Lambda} \tag{4.2}$$

To eliminate the dependence of conserved variables $\mathbf{Q}$ on the design variables, we solve the adjoint equation

$$\left[\frac{\partial \mathbf{R}}{\partial \mathbf{Q}}\right]^T \mathbf{\Lambda} = -\frac{\partial f}{\partial \mathbf{Q}} \tag{4.3}$$

Where the Lagrange multipliers (also known as costate variables), $\mathbf{\Lambda}$ are the cost function dependence on the residual

$$\mathbf{\Lambda} = -\frac{\partial f}{\partial \mathbf{R}} \tag{4.4}$$

This can ultimately be used in error estimation and sensitivity analysis for design optimization. With the second term in Eq. 4.2 eliminated, the derivative of the Lagrangian becomes

$$\frac{\partial L}{\partial \mathbf{D}} = \left\{ \frac{\partial f}{\partial \mathbf{D}} + \left[\frac{\partial \mathbf{X}}{\partial \mathbf{D}}\right]^T \frac{\partial f}{\partial \mathbf{X}} \right\} + \left\{ \left[\frac{\partial \mathbf{R}}{\partial \mathbf{D}}\right]^T + \left[\frac{\partial \mathbf{X}}{\partial \mathbf{D}}\right]^T \left[\frac{\partial \mathbf{R}}{\partial \mathbf{X}}\right]^T \right\} \mathbf{\Lambda} \tag{4.5}$$

By solving the adjoint equation in Eq. 4.3) to obtain the costate variable vector, $\mathbf{\Lambda}$, we can now use a non-linear optimizer to determine the optimum set of design variables, $\mathbf{D}^*$. This can be done using **SNOPT[17]**, **KSOPT[22]**, or **NPSOL[16]** in FUN3D, as well as a host of other non-linear optimizers.

4.2 Block Jacobi Adjoint Decoupling

It is possible to decoupled the adjoint equations in a fashion similar to that done to the primal flow equations. In this decoupled adjoint formulation, the conserved variables are split identically to flow equations, with the fully-coupled vector of conserved variables

$$\mathbf{U} = \begin{pmatrix} \rho_1 \\ \vdots \\ \rho_{ns} \\ \rho\mathbf{u} \\ \rho E \end{pmatrix} \tag{4.6}$$

split into

$$\mathbf{U}' = \begin{pmatrix} \rho \\ \rho\mathbf{u} \\ \rho E \end{pmatrix}, \qquad \hat{\mathbf{U}} = \begin{pmatrix} \rho_1 \\ \vdots \\ \rho_{ns} \end{pmatrix} \tag{4.7}$$

With this splitting, the mixture equations for single point in the global system of the decoupled flow solve can be written as

$$\frac{V}{\Delta t}\mathbf{I} + \begin{pmatrix} \frac{\partial \mathbf{R}_\rho}{\partial \rho} & \frac{\partial \mathbf{R}_\rho}{\partial \rho \mathbf{u}} & \frac{\partial \mathbf{R}_\rho}{\partial \rho E} \\[2ex] \frac{\partial \mathbf{R}_{\rho \mathbf{u}}}{\partial \rho} & \frac{\partial \mathbf{R}_{\rho \mathbf{u}}}{\partial \rho \mathbf{u}} & \frac{\partial \mathbf{R}_{\rho \mathbf{u}}}{\partial \rho E} \\[2ex] \frac{\partial \mathbf{R}_{\rho E}}{\partial \rho} & \frac{\partial \mathbf{R}_{\rho E}}{\partial \rho \mathbf{u}} & \frac{\partial \mathbf{R}_{\rho E}}{\partial \rho E} \end{pmatrix} \begin{pmatrix} \Delta \rho \\[2ex] \Delta \rho \mathbf{u} \\[2ex] \Delta \rho E \end{pmatrix} = \begin{pmatrix} \mathbf{R}_\rho \\[2ex] \mathbf{R}_{\rho \mathbf{u}} \\[2ex] \mathbf{R}_{\rho E} \end{pmatrix} \tag{4.8}$$

Likewise, the species mass equations for a single point can be written as

$$\frac{V}{\Delta t}\mathbf{I} + \begin{pmatrix} \frac{\partial \mathbf{R}_{\rho_1}}{\partial c_1} & \cdots & \frac{\partial \mathbf{R}_{\rho_1}}{\partial c_{ns}} \\[2ex] \vdots & \ddots & \vdots \\[2ex] \frac{\partial \mathbf{R}_{\rho_{ns}}}{\partial c_1} & \cdots & \frac{\partial \mathbf{R}_{\rho_{ns}}}{\partial c_{ns}} \end{pmatrix} \begin{pmatrix} \Delta c_1 \\[2ex] \vdots \\[2ex] \Delta c_{ns} \end{pmatrix} = \begin{pmatrix} \mathbf{R}_{\rho_1} \\[2ex] \vdots \\[2ex] \mathbf{R}_{\rho_{ns}} \end{pmatrix} \tag{4.9}$$

Examining Eq.s (4.8-4.9) shows that there are clearly some physical dependencies being omitted, namely $\frac{\partial \mathbf{R}_{\rho_i}}{\partial \rho}$, $\frac{\partial \mathbf{R}_\rho}{\partial c_j}$, $\frac{\partial \mathbf{R}_{\rho \mathbf{u}}}{\partial c_j}$, and $\frac{\partial \mathbf{R}_{\rho E}}{\partial c_j}$. It has been found[9] that omitting these dependencies does not hinder convergence the primal flow solver; however, because the adjoint requires an exact linearization of the converged steady-state solution, these must be accounted for in the decoupled adjoint formulation.

The next step is to reconcile the split conserved variables, $\mathbf{U}'$ and $\hat{\mathbf{U}}$, with the conserved variable vector $\mathbf{Q}$ in the discrete adjoint formulation given in Eq. 4.3. The most intuitive and straightforward way to do this is to forgo solving for the species mass ρ_i in lieu of the species mass fraction c_i. Thus, $\mathbf{Q}$ can be expressed as

$$\mathbf{Q} = \begin{pmatrix} \rho \\ \rho u \\ \rho v \\ \rho w \\ \rho E \\ c_1 \\ \vdots \\ c_{ns} \end{pmatrix} \tag{4.10}$$

This allows the linearizations in Eq.s (4.8-4.9) to be used in the adjoint formulation, by augmenting them with the previously omitted linearizations. Replacing $\frac{\partial \mathbf{R}}{\partial \mathbf{Q}}$ with the fully-coupled

system, the adjoint system becomes

$$
\begin{pmatrix}
\frac{\partial \mathbf{R}_\rho}{\partial \rho}^T & \frac{\partial \mathbf{R}_{\rho\mathbf{u}}}{\partial \rho}^T & \frac{\partial \mathbf{R}_{\rho E}}{\partial \rho}^T & \frac{\partial \mathbf{R}_{\rho_i}}{\partial \rho}^T \\[2mm]
\frac{\partial \mathbf{R}_\rho}{\partial \rho\mathbf{u}}^T & \frac{\partial \mathbf{R}_{\rho\mathbf{u}}}{\partial \rho\mathbf{u}}^T & \frac{\partial \mathbf{R}_{\rho E}}{\partial \rho\mathbf{u}}^T & \frac{\partial \mathbf{R}_{\rho_i}}{\partial \rho\mathbf{u}}^T \\[2mm]
\frac{\partial \mathbf{R}_\rho}{\partial \rho E}^T & \frac{\partial \mathbf{R}_{\rho\mathbf{u}}}{\partial \rho E}^T & \frac{\partial \mathbf{R}_{\rho E}}{\partial \rho E}^T & \frac{\partial \mathbf{R}_{\rho_i}}{\partial \rho E}^T \\[2mm]
\frac{\partial \mathbf{R}_\rho}{\partial c_j}^T & \frac{\partial \mathbf{R}_{\rho\mathbf{u}}}{\partial c_j}^T & \frac{\partial \mathbf{R}_{\rho E}}{\partial c_j}^T & \frac{\partial \mathbf{R}_{\rho_i}}{\partial c_j}^T
\end{pmatrix}
\begin{pmatrix}
\Lambda_\rho \\[2mm]
\Lambda_{\rho\mathbf{u}} \\[2mm]
\Lambda_{\rho E} \\[2mm]
\Lambda_{c_i}
\end{pmatrix}
= -
\begin{pmatrix}
\frac{\partial f}{\partial \rho} \\[2mm]
\frac{\partial f}{\partial \rho\mathbf{u}} \\[2mm]
\frac{\partial f}{\partial \rho E} \\[2mm]
\frac{\partial f}{\partial c_j}
\end{pmatrix}
\tag{4.11}
$$

Thus the Jacobian in Eq. 4.11 is the completed one of Eq.s (4.8-4.9). While this is useful, the advantage of decoupling the species equations from the mixture equations was to speed up the linear solver and save memory. Solving Eq. 4.11 is roughly equivalent to solving the fully-coupled system of equations, which undermines both of these goals; so, an alternative solution strategy must be formulated. If a block Jacobi scheme is employed, the system can be decoupled once again as

$$
\begin{pmatrix}
\frac{\partial \mathbf{R}_\rho}{\partial \rho}^T & \frac{\partial \mathbf{R}_{\rho\mathbf{u}}}{\partial \rho}^T & \frac{\partial \mathbf{R}_{\rho E}}{\partial \rho}^T \\[2mm]
\frac{\partial \mathbf{R}_\rho}{\partial \rho\mathbf{u}}^T & \frac{\partial \mathbf{R}_{\rho\mathbf{u}}}{\partial \rho\mathbf{u}}^T & \frac{\partial \mathbf{R}_{\rho E}}{\partial \rho\mathbf{u}}^T \\[2mm]
\frac{\partial \mathbf{R}_\rho}{\partial \rho E}^T & \frac{\partial \mathbf{R}_{\rho\mathbf{u}}}{\partial \rho E}^T & \frac{\partial \mathbf{R}_{\rho E}}{\partial \rho E}^T
\end{pmatrix}
\begin{pmatrix}
\Lambda_\rho \\[2mm]
\Lambda_{\rho\mathbf{u}} \\[2mm]
\Lambda_{\rho E}
\end{pmatrix}
= -
\begin{pmatrix}
\frac{\partial f}{\partial \rho} \\[2mm]
\frac{\partial f}{\partial \rho\mathbf{u}} \\[2mm]
\frac{\partial f}{\partial \rho E}
\end{pmatrix}
-
\begin{pmatrix}
\frac{\partial \mathbf{R}_{\rho_i}}{\partial \rho}^T \\[2mm]
\frac{\partial \mathbf{R}_{\rho_i}}{\partial \rho\mathbf{u}}^T \\[2mm]
\frac{\partial \mathbf{R}_{\rho_i}}{\partial \rho E}^T
\end{pmatrix}
\Lambda_{c_i}
\tag{4.12}
$$

$$
\frac{\partial \mathbf{R}_{\rho_i}}{\partial c_j}^T \Lambda_{c_i} = -\frac{\partial f}{\partial c_j} - \frac{\partial \mathbf{R}_\rho}{\partial c_j}^T \Lambda_\rho - \frac{\partial \mathbf{R}_{\rho\mathbf{u}}}{\partial c_j}^T \Lambda_{\rho\mathbf{u}} - \frac{\partial \mathbf{R}_{\rho E}}{\partial c_j}^T \Lambda_{\rho E}
\tag{4.13}
$$

Adding a time-like derivative to the adjoint equations, the solution of the costate variables, Λ, can be time marched similar to the primal flow solver

$$
\left[\frac{V}{\Delta t} \mathbf{I} + \frac{\partial \mathbf{R}}{\partial \mathbf{Q}}^T \right] \Delta \Lambda = -\frac{\partial f}{\partial \mathbf{Q}} - \frac{\partial \mathbf{R}}{\partial \mathbf{Q}}^T \Lambda
\tag{4.14}
$$

20

Thus, the first system of equations in Eq. 4.12 becomes

$$
\left[\frac{V}{\Delta t}\mathbf{I} + \begin{pmatrix} \frac{\partial \mathbf{R}_\rho}{\partial \rho}^T & \frac{\partial \mathbf{R}_{\rho\mathbf{u}}}{\partial \rho}^T & \frac{\partial \mathbf{R}_{\rho E}}{\partial \rho}^T \\ \frac{\partial \mathbf{R}_\rho}{\partial \rho\mathbf{u}}^T & \frac{\partial \mathbf{R}_{\rho\mathbf{u}}}{\partial \rho\mathbf{u}}^T & \frac{\partial \mathbf{R}_{\rho E}}{\partial \rho\mathbf{u}}^T \\ \frac{\partial \mathbf{R}_\rho}{\partial \rho E}^T & \frac{\partial \mathbf{R}_{\rho\mathbf{u}}}{\partial \rho E}^T & \frac{\partial \mathbf{R}_{\rho E}}{\partial \rho E}^T \end{pmatrix}\right] \begin{pmatrix} \Delta\Lambda_\rho \\ \Delta\Lambda_{\rho\mathbf{u}} \\ \Delta\Lambda_{\rho E} \end{pmatrix} =
$$
$$
- \begin{pmatrix} \frac{\partial f}{\partial \rho} \\ \frac{\partial f}{\partial \rho\mathbf{u}} \\ \frac{\partial f}{\partial \rho E} \end{pmatrix} - \begin{pmatrix} \frac{\partial \mathbf{R}_\rho}{\partial \rho}^T & \frac{\partial \mathbf{R}_{\rho\mathbf{u}}}{\partial \rho}^T & \frac{\partial \mathbf{R}_{\rho E}}{\partial \rho}^T \\ \frac{\partial \mathbf{R}_\rho}{\partial \rho\mathbf{u}}^T & \frac{\partial \mathbf{R}_{\rho\mathbf{u}}}{\partial \rho\mathbf{u}}^T & \frac{\partial \mathbf{R}_{\rho E}}{\partial \rho\mathbf{u}}^T \\ \frac{\partial \mathbf{R}_\rho}{\partial \rho E}^T & \frac{\partial \mathbf{R}_{\rho\mathbf{u}}}{\partial \rho E}^T & \frac{\partial \mathbf{R}_{\rho E}}{\partial \rho E}^T \end{pmatrix} \begin{pmatrix} \Lambda_\rho \\ \Lambda_{\rho\mathbf{u}} \\ \Lambda_{\rho E} \end{pmatrix} - \begin{pmatrix} \frac{\partial \mathbf{R}_{\rho_i}}{\partial \rho}^T \\ \frac{\partial \mathbf{R}_{\rho_i}}{\partial \rho\mathbf{u}}^T \\ \frac{\partial \mathbf{R}_{\rho_i}}{\partial \rho E}^T \end{pmatrix} \Lambda_{c_i} \quad (4.15)
$$

and the second system in Eq. 4.13 becomes

$$
\left(\frac{V}{\Delta t}\mathbf{I} + \frac{\partial \mathbf{R}_{\rho_i}}{\partial c_j}^T\right)\Delta\Lambda_{c_i} = -\frac{\partial f}{\partial c_j} - \frac{\partial \mathbf{R}_{\rho_i}}{\partial c_j}^T \Lambda_{c_i} - \frac{\partial \mathbf{R}_\rho}{\partial c_j}^T \Lambda_\rho - \frac{\partial \mathbf{R}_{\rho\mathbf{u}}}{\partial c_j}^T \Lambda_{\rho\mathbf{u}} - \frac{\partial \mathbf{R}_{\rho E}}{\partial c_j}^T \Lambda_{\rho E} \quad (4.16)
$$

The LHS of Eq.s (4.15-4.16) are the same first-order approximate Jacobians that were used to solve the primal flow equations; therefore, all of the benefits of the diagonal block matrices that are exploited in the primal flow solver to reduce the linear solver cost and overall memory now apply to the adjoint.

4.3   Higher-order Reconstruction Linearizations

To achieve higher-order accuracy, the FUN3D solver uses an extension of the unstructured MUSCL (U-MUSCL) reconstruction scheme developed by Burg et al[7, 8], which is itself and extension of the Monotonic Upstream-centered Scheme for Conservation Laws (MUSCL) scheme developed by Van Leer[35]. The implementation is a combination of central differencing and the original U-MUSCL scheme

$$
q_L = q_1 + (1 - \kappa)\left[\phi\left(\frac{\partial q_1}{\partial x}dx + \frac{\partial q_1}{\partial y}dy + \frac{\partial q_1}{\partial z}dz\right)\right] + \frac{\kappa}{2}(q_2 - q_1)
$$
$$
q_R = q_2 + (1 - \kappa)\left[\phi\left(\frac{\partial q_2}{\partial x}dx + \frac{\partial q_2}{\partial y}dy + \frac{\partial q_2}{\partial z}dz\right)\right] + \frac{\kappa}{2}(q_1 - q_2)
$$
(4.17)

Figure 4.1 shows that $q_{L,R}$ are the primitive variables at the left and right sides of the edge midpoint, where the flux is evaluated, $q_{1,2}$ are the primitive variables at nodes 1 and 2. The variable ϕ is the result of the modified Van Albada flux limiter function[34], and varies between
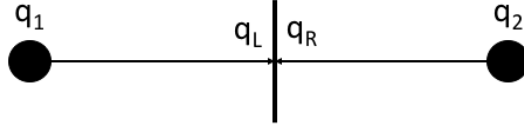
Figure 4.1: Edge Reconstruction

0 and 1 (effectively blending first-order and second order contributions to the flux evaluation). The adjoint uses a frozen flux limiter, for purposes that will be discussed in a later section, and is therefore held as constant in the linearization computations. Finally the gradient information $\frac{\partial q_{1,2}}{\partial x}$, $\frac{\partial q_{1,2}}{\partial y}$, and $\frac{\partial q_{1,2}}{\partial z}$ are computed using least-squares. For the example 2-D stencil shown in Figure 4.2 this is effectively computed as

$$
\begin{aligned}
\frac{\partial q}{\partial x} &= \sum_{i=1}^{5} W_{x,i} \left(q_i - q_0 \right) \\
\frac{\partial q}{\partial y} &= \sum_{i=1}^{5} W_{y,i} \left(q_i - q_0 \right) \\
\frac{\partial q}{\partial z} &= \sum_{i=1}^{5} W_{z,i} \left(q_i - q_0 \right)
\end{aligned}
\tag{4.18}
$$

where the z direction would come from geometry out of the page. In practice, the higher order

Figure 4.2: Example Stencil for Least-Squares Gradient Evaluation

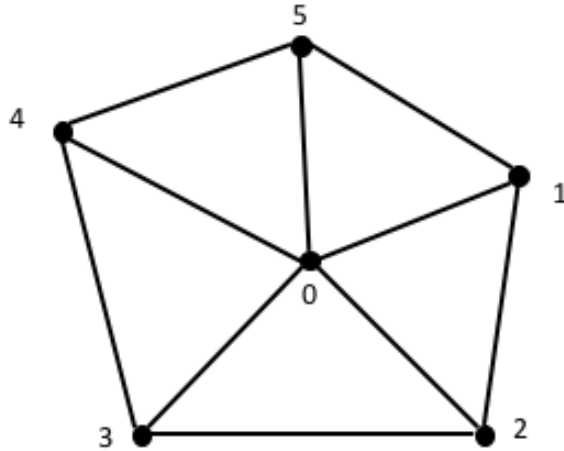linearizations can be managed easily by constructing a list of neighboring nodes for each node. By the chain rule the linearization of the residual, R, is then evaluated in two parts

$$\frac{\partial \mathbf{R}\left(\mathbf{Q}^*\left(\mathbf{Q}\right)\right)}{\partial \mathbf{Q}} = \frac{\partial \mathbf{R}}{\partial \mathbf{Q}} + \frac{\partial \mathbf{R}}{\partial \mathbf{Q}^*}\frac{\partial \mathbf{Q}^*}{\partial \mathbf{Q}}$$

(4.19)

where $\mathbf{Q}$ are the conserved variables at each node, and $\mathbf{Q}^*$ are the higher order terms computed in the U-MUSCL reconstruction; therefore, after computing the exact Jacobian of the Roe FDS scheme, $\frac{\partial \mathbf{R}}{\partial \mathbf{Q}}$, the higher order linearization is computed by making a circuit around each node to pick up the contributions from the least squares gradient computation. For the example stencil in Figure 4.2, the contribution to the residual from looping around node 0 would be

$$\frac{\partial \mathbf{R}_0}{\partial \mathbf{Q}^*}\frac{\partial \mathbf{Q}^*}{\partial \mathbf{Q}_0} = \frac{\partial \mathbf{R}_0}{\partial \mathbf{Q}^*}\left[\sum_{i=1}^{5}\left(1-\kappa\right)\left(-W_{x,i}dx - W_{y,i}dy - W_{z,i}dz\right)\frac{\partial q_0}{\partial \mathbf{Q}_0}\right]$$

(4.20)

An important point that this illustrates is that the linearization of the higher order terms is not dependent upon the choice of the primitive variable vector q, provided that all of the linearizations are exact. This is powerful, because it allows the decoupled scheme to be extended to higher work, without needing to reformulate the linearizations drastically from the fully-coupled scheme.

Chapter 5

Design Optimization

Design optimization is a wide field that encompasses methods generally falling into two categories: local gradient-based optimization, and heuristic global optimization. Local gradient-based optimization techniques focus on the determining an optimality condition by evaluating a function and its gradients. Provided certain conditions are met, it can be proven that the optimization procedure will find a local minimum or maximum on a bounded domain. Examples of local gradient-based optimization methods include steepest-descent[13], sequential quadratic programming (SQP)[15], as well as an interesting method that converts a constrained optimization problem into an unconstrained on by employing the Kreisselmeier-Steinhauser function[36]. A heuristic global optimization seeks to find the global extrema of a function. Although these methods are powerful, because of their heuristic nature they are not guaranteed to find the absolute optimum condition and are not the focus this research.

In the field of optimization, the function of interest is referred to as the "cost function" or "objective function". Optimization methods seek to minimize this function; therefore, if the intent is to find the maximum value of the function, it should be formulated as the negative of the original. This section focuses on geometry and test conditions for the optimization, the implementation of the cost function components and design variables used in the optimization, as well as the interface to the optimizer that is used.

5.1   Annular Jet Configuration and Test Conditions

This design optimization is intended to showcase the adjoint-based formulation used to obtain sensitivity information. The geometry chosen is a hypersonic re-entry vehicle with an annular nozzle, as shown in Figure 5.1. This geometry was originally investigated by Gnoffo et al[19] to obtain increased drag from "pulsing" the annular jet to obtain a beneficial effect from the unsteady shock interaction with the plume of the jet. For this work, the optimization is con-
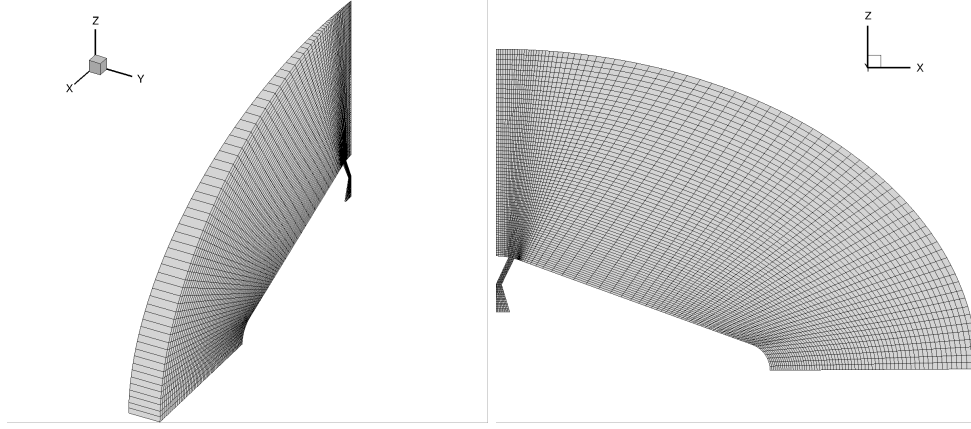
Figure 5.1: Annular Jet Geometry

ducted for purely steady flow, with the intent of altering the plenum conditions to achieve the optimum condition of maximizing drag, while minimizing surface temperature.

The geometry was generated with the parameters shown in Table 5.1, with the mesh originally created as structured grid and then converted to an unstructured grid of hexahedra elements. The flow conditions for the optimization are shown in Table 5.2

Parameter	Description	Value
r_{throat}	nozzle throat radius, m	0.02
r_{plenum}	nozzle radius at plenum face, m	0.05
$r_{exit,inner}$	inside nozzle radius at exit, m	0.03
$r_{exit,outer}$	outside nozzle radius at exit, m	0.05
l_{conv}	distance from plenum to throat, m	0.05
θ_c	cone half angle, deg	70.0

Table 5.1: Annular Nozzle Geometry Inputs

Flow Condition	Description	Value
V_∞	freestream velocity, m/s	5686.24
ρ_∞	freestream density, kg/m^3	0.001
T_∞	freestream temperature, K	200.0
M_∞	freestream Mach number (derived)	20.0

Table 5.2: Flow Conditions

5.2 Cost Function Definition

The cost function (or objective function) as formulated in FUN3D is a composite, weighted function

$$f = \sum_{j=1}^{N_{func}} w_j \left(C_j - C_{j*} \right)^{p_j} \tag{5.1}$$

Where w_j, C_{j*}, and p_j are the weight, target, and power of cost function component j. C_j is the component value, which is evaluated at each flow solution. For this particular optimization problem the cost function is defined as

$$f = w_1 \left(T_{RMS} \right)^2 + w_2 \left(C_D - C_D^* \right)^2 \tag{5.2}$$

The component weights were determined heuristically, to normalize the changes in drag coefficient, C_D, and surface temperature Root-Mean-Square (RMS) T_{RMS}. The drag coefficient is defined as

$$C_D = \sum_i^{N_{faces}} \frac{2 \left(p_i - p_\infty \right) n_{x_i}}{\rho_\infty V_\infty S_{ref}} \tag{5.3}$$

where p_i is the average pressure at face i. RMS of surface temperature is defined as

$$\sqrt{\frac{\sum_i^{N_{faces}} \left(T_{RMS} A_i \right)^2}{\sum_i^{N_{faces}} \left(A_i \right)^2}} \tag{5.4}$$

The area-weighted RMS of surface temperature was chosen over a simple area-weighted average of surface temperature, because the stagnation temperature is generally much higher than temperature elsewhere on a vehicle forebody in hypersonic flows; therefore, the squaring of temperature in the RMS will give greater weight to the stagnation temperature in the design.

A primary objective of this optimization is to explore the effects of the plume from the annular jet interacting with the bow shock; thus, the thrust effects and, therefore, forces inside the nozzle are ignored. To accomplish this, only the area shown in Figure 5.2a is integrated to compute the drag coefficient and surface temperature RMS.

5.3 Design Variables

The design variables for the optimization problem are the plenum total pressure, $P_{p,o}$, and plenum total temperature, $T_{p,o}$. These are provided explicitly in the optimization problem, and are used to directly set the flow conditions on plenum face boundary condition in the nozzle, shown in Figure 5.2b. For a reacting gas mixture, mass fractions for species leaving the plenum

(a) C_D and T_{RMS} Integrated Area   (b) Plenum Face Boundary Condition
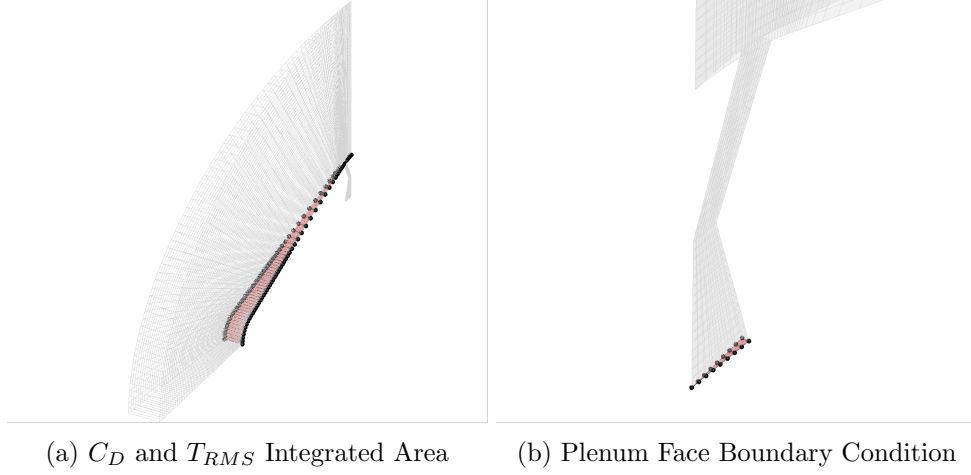
can also be specified as a design variable.

The sensitivity gradients for these design variables are easily obtained by manipulating Eq. 4.5 to obtain

$$\frac{\partial L}{\partial \mathbf{D}} = \frac{\partial f}{\partial \mathbf{D}} + \frac{\partial \mathbf{R}}{\partial \mathbf{Q}}^T \mathbf{\Lambda} \tag{5.5}$$

Thus once the adjoint co-state variables $\mathbf{\Lambda}$ has been computed by by solving the adjoint equations (Eq. 4.3) the sensitivity derivatives for C_D and T_{RMS} on the specified surfaces are obtained by evaluating relatively inexpensive matrix-vector products.

Chapter 6

Verification of Adjoint Sensitivity Gradients

In this section the sensitivity gradients computed by the adjoint-formulation are verified against finite-difference derivatives with a complex step. This details the methods by which the gradient information is computed in the forward-mode and in the reverse-mode.

6.1 Forward-mode Sensitivities Using Complex-Variables

The sensitivities can be computed in the forward-mode by using finite-difference. While this approach is unfavorable to use in practice, because a minimum number of flow solves equivalent to the number of design variables are required, it is a straight-forward way to verify that sensitivities computed by the adjoint solver are correct. To avoid cancellation errors associated with real-variable finite difference, an approach that uses complex variables was originally suggested by Squire and Trapp[32] and evaluated by Newman et al[26]. This complex-variable approach can be used to determine the derivative of a real valued function, f, by considering the Taylor series expansion of f using a complex step ih

$$f(x + ih) = \sum_{k=0} \left(\frac{(ih)^k}{!k} \frac{\partial^k f}{\partial x^k} \right) = f(x) + ih \frac{\partial f}{\partial x} - \frac{h^2}{2} \frac{\partial^2 f}{\partial x^2} - \frac{h^3}{6} \frac{\partial^3 f}{\partial x^3} + \cdots \qquad (6.1)$$

taking the imaginary parts of both sides of Eq. 6.1 and solving for the first derivative yields

$$\begin{aligned}
\frac{\partial f}{\partial x} &= \frac{Im\left[f(x + ih)\right]}{h} - \frac{h^2}{6} \frac{\partial^3 f}{\partial x^3} \\
&= \frac{Im\left[f(x + ih)\right]}{h} - O(h^2)
\end{aligned} \qquad (6.2)$$

Thus, this complex-variable approach provides a means of computing the cost function derivatives without subtractive cancellation error, giving truly second order accuracy. The power of using this approach is that the derivative of any function with respect to a single can be computed without any additional work, other than the function be made to use complex arithmetic and a complex-valued perturbation be applied.

In practice, this complex-variable approach is implemented by transforming the source code such that all real variables used in a function evaluation are made to be complex variables. A specified step size is then added to the complex part of the design variable that the cost function is to be linearized with respect to in the function evaluation. Provide the "complexified" solver converges in the same manner as the real-variable solver, the complex part of the function of interest is the sensitivity derivative.

As mentioned before, the complex-variable and real-variable solvers must converge to the same solution for the comparison between the adjoint-computed sensitivity derivatives and those computed by the complex-variable approach to be valid. The use of a flux limiter is mandatory for hypersonic applications, where strong shocks are present; however, the solver is very sensitive to changes in the reconstruction, and a "ringing" of the residual is often observed[18] when using a flux limiter in FUN3D. While this sub-convergence of the conservation equation residuals is not detrimental to the primal flow solver results, as most aerothermodynamic quantities are usually sufficiently converged by this point, the adjoint-formulation is predicated on the residual being zero, or at least nearly zero. Because of this last point, the stalled convergence can cause the adjoint solver to give incorrect results or cause the adjoint solution to diverge. To prevent this, the adjoint is required to be run with a "frozen" limiter, that is only where a reconstruction is unrealisable is the value of the limiter function changed. Doing this usually results in the residuals converging to machine precision.

A significant obstacle with using a frozen limiter is that the real-variable and complex-variable solvers do not freeze the limiter identically. Although the solvers are nearly identically, their floating-point operations will be different since complex arithmetic is involved in only the complex-variable solver. The flux limiter formulation is sensitive to these differences and will result in a different converged state, regardless of the limiter being frozen at the same iteration between the solvers. To overcome this, the complex-variable solver must not be allowed to change the value of the flux limiter. To implement this, the solution is converged to machine precision with the real-variable solver and then the complex-variable solver is started with the flow field of the converged real-variable solution. The complex step is then added to the design variable; however, the flux limiter is frozen. Because limiter value is constant, the real solution from the complex-variable and real-variable solutions will match identically, and the complex part of the solution will be converged without ever needing to update the flux limiter. This will ensure that the sensitivity derivatives from the complex and adjoint solvers match to high

precision for hypersonic cases with a frozen flux limiter.

6.2 Verification of 2nd-order Adjoint Linearizations

To verify the hand-coded linearizations implemented in the adjoint solver, the derivatives of the drag and surface temperature cost functions for the annular nozzle geometry were computed using both the adjoint method and the complex-variable approach. Using the adjoint solution derivatives with respect to the plenum pressure and plenum temperature design variables are computed by Eq. 5.5

REFERENCES

[1] ACM SIGPLAN 2007 Conference on Programing Language Design and Implementation. *How to Shadow Every Byte of Memory Used by a Program*, San Diego, CA, June 2007.

[2] W. K. Anderson and D. L. Bonhaus. "an implicit upwind algorithm for computing turbulent flows on unstructured grids". *Computers and Fluids*, 23(1):1–22, 1994.

[3] Dinesh Balagangadhar and Subrata Roy. Design sensitivity analysis and optimization of steady fluid-thermal systems. *Computer Methods in Applied Mechanics and Engineering*, 190(42):5465–5479, 2001.

[4] Robert Bartels, Veer Vatsa, Jan-Renee Carlson, and Raymond Mineck. Fun3d grid refinement and adaptation studies for the ares launch vehicle. In *28th AIAA Applied Aerodynamics Conference*. AIAA, 2015/10/06 2010.

[5] Oktay Baysal and Mohamed E Eleshaky. Aerodynamic design optimization using sensitivity analysis and computational fluid dynamics. *AIAA journal*, 30(3):718–725, 1992.

[6] Martin A. Reno Bonnie J. McBride, Sanford Gordon. Coefficients for calculating thermodynamic and transport properties of individual species. Technical report, NASA, 1993.

[7] Clarence OE Burg. Higher order variable extrapolation for unstructured finite volume rans flow solvers. *AIAA Paper*, 4999:2005, 2005.

[8] Clarence OE Burg, Chunhua Sheng, James C Newman III, Wesley Brewer, Eric Blades, and David L Marcum. Verification and validation of forces generated by an unstructured flow solver. *AIAA paper*, 3983:2003, 2003.

[9] Graham V. Candler, Pramod K. Subbareddy, and Ioannis Nompelis. Decoupled implicit method for aerothermodynamics and reacting flows. *AIAA Journal*, 51(5):1245–1254, 2015/04/23 2013.

[10] Sean R. Copeland, Francisco Palacios, and Juan J. Alonso. Adjoint-based aerothermodynamic shape design of hypersonic vehicles in non-equilibrium flows. In *52nd Aerospace Sciences Meeting*. American Institute of Aeronautics and Astronautics, 2014.

[11] Mohammad K. Esfahani and Guillaume Houzeaux. Implementation of discrete adjoint method for parameter sensitivity analysis in chemically reacting flows. In *57th AIAA/ASCE/AHS/ASC Structures, Structural Dynamics, and Materials Conference*. American Institute of Aeronautics and Astronautics, 2016/09/20 2016.

[12] Paul F. Fischer. *Scaling Limits for PDE-Based Simulation (Invited)*. American Institute of Aeronautics and Astronautics, 2015/10/21 2015.

[13] Roger Fletcher and Michael JD Powell. A rapidly convergent descent method for minimization. *The Computer Journal*, 6(2):163–168, 1963.

[14] Alan George and Joseph W. Liu. *Computer Solution of Large Sparse Positive Definite.* Prentice Hall Professional Technical Reference, 1981.

[15] Philip E. Gill, Walter Murray, and Michael A. Saunders. Snopt: An sqp algorithm for large-scale constrained optimization. *SIAM Review*, 47(1):99–131, 2005.

[16] Philip E. Gill, Elizabeth Wong, Walter Murray, and Michael Saunders. *User's Guide for NPSOL 5.0: A FORTRAN Package for Nonlinear Programming*, July 1998.

[17] Philip E. Gill, Elizabeth Wong, Walter Murray, and Michael Saunders. *User's Guide for SNOPT Version 7.4: Software Large-Scale Nonlinear Programming*, January 2015.

[18] Peter A Gnoffo. Simulation of stagnation region heating in hypersonic flow on tetrahedral grids. *AIAA Paper*, 3960(7):52, 2007.

[19] Peter A Gnoffo, Kyle Thompson, and Ashley Korzun. Tapping the brake for entry, descent, and landing. In *46th AIAA Fluid Dynamics Conference*, page 4277, 2016.

[20] R. N.; Gnoffo, P. A.; Gupta and J. L. Shinn. Conservation equations and physical models for hypersonic air flows in thermal and chemical nonequilibrium. Technical Paper 2867, NASA, 1989.

[21] Ami Harten. High resolution schemes for hyperbolic conservation laws. *Journal of Computational Physics*, 49(3):357–393, 1983.

[22] P.W. Jansen and R.E. Perez. Constrained structural design optimization via a parallel augmented lagrangian particle swarm optimization approach. *Computers & Structures*, 89(13–14):1352 – 1366, 2011.

[23] Robert W. MacCormack and Graham V. Candler. The solution of the navier-stokes equations using gauss-seidel line relaxation. *Computers and Fluids*, 17(1):135–150, 1989.

[24] Dimitri J. Mavriplis. Multigrid solution of the discrete adjoint for optimization problems on unstructured meshes. *AIAA Journal*, 44(1):42–50, January 2006.

[25] Marian Nemec, Michael J. Aftosmis, Scott M. Murman, and Thomas H. Pulliam. Adjoint formulation for an embedded-boundary cartesian method. AIAA Paper 2005–877, 2005.

[26] James C Newman, W Kyle Anderson, and David L Whitfield. Multidisciplinary sensitivity derivatives using complex variables. *Mississippi State University Publication, MSSU-EIRS-ERC-98-08*, 1998.

[27] Eric J Nielsen and W Kyle Anderson. Recent improvements in aerodynamic design optimization on unstructured meshes. *AIAA journal*, 40(6):1155–1163, 2002.

[28] Chul Park. On convergence of computation of chemically reacting flows. In *AIAA, Aerospace Sciences Meeting*, volume 1, 1985.

[29] Chul Park. Assessment of two-temperature kinetic model for ionizing air. *Journal of Thermophysics and Heat Transfer*, 3(3):233–244, 1989.

[30] P.L Roe. Approximate riemann solvers, parameter vectors, and difference schemes. *Journal of Computational Physics*, 43(2):357 – 372, 1981.

[31] Y. Saad. *Iterative Methods for Sparse Linear Systems*, pages 391–392. Society for Industrial and Applied Mathematics, 2003.

[32] William Squire and George Trapp. Using complex variables to estimate derivatives of real functions. *Siam Review*, 40(1):110–112, 1998.

[33] Joseph L Steger and R.F Warming. Flux vector splitting of the inviscid gasdynamic equations with application to finite-difference methods. *Journal of Computational Physics*, 40(2):263 – 293, 1981.

[34] GD Van Albada, Bram Van Leer, and WW Roberts Jr. A comparative study of computational methods in cosmic gas dynamics. In *Upwind and High-Resolution Schemes*, pages 95–103. Springer, 1997.

[35] Bram Van Leer. Towards the ultimate conservative difference scheme. v. a second-order sequel to godunov's method. *Journal of computational Physics*, 32(1):101–136, 1979.

[36] Gregory A Wrenn. An indirect method for numerical optimization using the kreisselmeir-steinhauser function. 1989.

APPENDIX

Appendix A

Derivations

A.1   Decoupled Flux Derivation

For the Roe flux difference splitting scheme, the species mass fluxes are given by

$$F_{\rho_s} = \frac{\rho_s^L \overline{U}^L + \rho_s^R \overline{U}^R}{2} - \frac{\tilde{c}_s(\lambda_1 dv_1 + \lambda_2 dv_2) + \lambda_3 dv_{3_s}}{2} \tag{A.1}$$

$$dv_1 = \frac{p^R - p^L + \tilde{\rho}\tilde{a}(\overline{U}^R - \overline{U}^L)}{\tilde{a}^2} \tag{A.2}$$

$$dv_2 = \frac{p^R - p^L - \tilde{\rho}\tilde{a}(\overline{U}^R - \overline{U}^L)}{\tilde{a}^2} \tag{A.3}$$

$$dv_{3_s} = \frac{\tilde{a}^2(\rho_s^R - \rho_s^L) - \tilde{c}_s(p^R - p^L)}{\tilde{a}^2} \tag{A.4}$$

$$\lambda_1 = |\ \overline{\mathbf{U}} + \tilde{a}\ |, \quad \lambda_2 = |\ \overline{\mathbf{U}} - \tilde{a}\ |, \quad \lambda_3 = |\ \overline{\mathbf{U}}\ | \tag{A.5}$$

where the ˜notation signifies a Roe-averaged quantity, given by:

$$\tilde{\mathbf{U}} = w\tilde{\mathbf{U}}^L + (1 - w)\tilde{\mathbf{U}}^R \tag{A.6}$$

$$w = \frac{\tilde{\rho}}{\tilde{\rho} + \rho^R} \tag{A.7}$$

$$\tilde{\rho} = \sqrt{\rho^R \rho^L} \tag{A.8}$$

The species mass fluxes must sum to the total mass flux; thus, the total mixture mass flux is given as

$$F_\rho = \sum_s F_{\rho_s} = \frac{\rho^L \overline{U}^L + \rho^R \overline{U}^R}{2} - \frac{\lambda_1 dv_1 + \lambda_2 dv_2 + \lambda_3 dv_3}{2} \tag{A.9}$$

$$dv_3 = \frac{\tilde{a}^2(\rho^R - \rho^L) - (p^R - p^L)}{\tilde{a}^2} \tag{A.10}$$

Multiplying Eq. (A.9) by the Roe-averaged mass fraction and substituting it into Eq. (A.1) results in:

$$F_{\rho_s} = \tilde{c}_s F_\rho + \frac{(c_s^L - \tilde{c}_s)\rho^L(\overline{U}^L + |\tilde{U}|)}{2} + \frac{(c_s^R - \tilde{c}_s)\rho^R(\overline{U}^R - |\tilde{U}|)}{2} \tag{A.11}$$

It should be noted here that the Roe-averaged normal velocity, $\tilde{U}$, requires an entropy correction in the presence of strong shocks[21]. This correction has a dependence on the roe-averaged speed of sound, and therefore has a dependence on the species mass fractions; however, through numerical experiments it has been determined that omitting this dependence does not adversely affect convergence. The notation can be further simplified by defining the normal velocities as follows:

$$\lambda^+ = \frac{\overline{U}^L + |\tilde{U}|}{2}, \quad \lambda^- = \frac{\overline{U}^R - |\tilde{U}|}{2} \tag{A.12}$$

Finally, substituting Eq. (A.12) into Eq. (A.11) yields the final result for calculating the species flux in the decoupled system:

$$F_{\rho_s} = \tilde{c}_s F_\rho + (c_s^L - \tilde{c}_s)\rho^L \lambda^+ + (c_s^R - \tilde{c}_s)\rho^R \lambda^- \tag{A.13}$$

Forming the convective contributions to the Jacobians is straightforward. Because the $\mathbf{U}'$ level variables are constant, only the left, right, and Roe-averaged state mass fractions vary. Differentiating Eq. (A.13) with respect to the mass fraction, c_s, the left and right state contributions are

$$\frac{\partial F_{\rho_s}}{\partial c_s^L} = w F_\rho + (1-w)\rho^L \lambda^+ - w\rho^R \lambda^- \tag{A.14}$$

$$\frac{\partial F_{\rho_s}}{\partial c_s^R} = (1-w)F_\rho + (w-1)\rho^L \lambda^+ + w\rho^R \lambda^- \tag{A.15}$$

Because there is no dependence between species in decoupled convective formulation, the Jacobian block elements are purely diagonal for the convective contributions, of the form

$$\begin{pmatrix} \frac{\partial F_{\rho_1}}{\partial c_1} & & 0 \\ & \ddots & \\ 0 & & \frac{\partial F_{\rho_{ns}}}{\partial c_{ns}} \end{pmatrix} \tag{A.16}$$

A.2 Quadratic Interpolation Between Thermodynamic Curve Fits

We seek to blend the two thermodynamic curve fits in such a way that we maintain c_0 continuity in both specific heat (C_p) and enthalpy (h). To accomplish this, a quadratic function must be used, of the form

$$aT^2 + bT + c = C_p \tag{A.17}$$

The coefficients a, b, and c are determined by solving the system that results from the boundary value problem

$$
\begin{cases}
aT_1{}^2 + bT_1 + c = C_{p_1} \\
aT_2{}^2 + bT_2 + c = C_{p_2} \\
a\frac{(T_2{}^3 - T_1{}^3)}{3} + b\frac{(T_2{}^2 - T_1{}^2)}{2} + c(T_2 - T_1) = h_2 - h_1
\end{cases}
\tag{A.18}
$$

Where the x_1 and x_2 subscripts describe the left and right states, respectively. Solving the linear system, the coefficients are

$$
\begin{cases}
fa = \frac{3(C_{p_2} + C_{p_1})}{(T_2 - T_1)^2} - \frac{6(h_2 - h_1)}{(T_2 - T_1)^3} \\[2ex]
b = -\frac{2[(C_{p_2} + 2C_{p_1})T_2 + (2C_{p_2} + C_{p_1})T_1]}{(T_2 - T_1)^2} + \frac{6(T_2 + T_1)(h_2 - h_1)}{(T_2 - T_1)^3} \\[2ex]
c = \frac{C_{p_1}T_2(T_2 + 2T_1) + C_{p_2}T_1(T_1 + 2T_2)}{(T_2 - T_1)^2} - \frac{6T_1 T_2(h_2 - h_1)}{(T_2 - T_1)^3}
\end{cases}
\tag{A.19}
$$

This can be simplified to

$$
\begin{cases}
a = 3B - A \\[2ex]
b = \frac{-2(C_{p_1}T_2 + C_{p_2}T_2)}{(T_2 - T_1)^2} + (T_2 + T_1)(A - 2B) \\[2ex]
c = \frac{C_{p_1}T_2{}^2 + C_{p_2}T_1{}^2}{(T_2 - T_1)^2} + T_1 T_2(2B - A)
\end{cases}
\tag{A.20}
$$

$$A = \frac{6(h_2 - h_1)}{(T_2 - T_1)^3} \tag{A.21}$$

$$B = \frac{C_{p_2} + C_{p_1}}{(T_2 - T_1)^2} \tag{A.22}$$

Note that this does not ensure that entropy will be continuous across curve fits.